Daily Flood Mapping at 90 m Resolution Through Physically-Constrained CYGNSS–SAR Fusion

Authors

Gauthier Malandrin
École Polytechnique, 91120 Palaiseau, France
Department of Civil and Environmental Engineering, University of California, Berkeley, CA 94720, USA

Cynthia Gerlein-Safdi (corresponding author)
Department of Civil and Environmental Engineering, University of California, Berkeley, CA 94720, USA
Lawrence Berkeley National Laboratory, Berkeley, CA 94720, USA
cgerlein@berkeley.edu

Preprint status

This is a non-peer-reviewed preprint submitted to EarthArXiv. This manuscript has been submitted to *IEEE Transactions on Geoscience and Remote Sensing* for peer review.

Code and data availability

Pre-trained model weights and inference code are publicly available at
https://github.com/gauthiermalandrin1903/cygnss-sar-flood-mapping
and
https://huggingface.co/gauthiermalandrin/cygnss-sar-flood-mapping

Daily Flood Mapping at 90 m Resolution Through Physically-Constrained CYGNSS–SAR Fusion

Gauthier Malandrin and Cynthia Gerlein-Safdi, *Member, IEEE*

***Abstract*—Satellite flood mapping faces a fundamental spatio-temporal trade-off: Synthetic Aperture Radar (SAR) missions provide high-resolution flood masks but revisit any given location only every 6–12 days, while GNSS Reflectometry observations from the CYGNSS constellation are available daily but at kilometer scale. Neither sensor alone suffices to track flood events evolving over 24–72 hours. We propose a physically-constrained deep learning framework that fuses daily CYGNSS inundation signals with Sentinel-1 SAR temporal anchors, conditioned on MERIT Hydro topographic variables, to produce daily flood maps at 90 m resolution. Flood observations are organized as temporal triplets (A→B→C), where B is the target date and A and C are SAR acquisitions bracketing B by 5–7 days. A temporal U-Net with three parallel encoding branches and learnable cross-attention gates fuses these inputs into spatially explicit flood probability maps. Trained and evaluated on a 47,653-tile dataset spanning seven flood-prone regions across three continents and seven years (2019–2025), the framework achieves a micro-averaged IoU of 0.703, outperforming the SAR-only state of the art (IoU = 0.67) despite solving a harder down-scaling problem. Ablation establishes that SAR temporal anchors dominate performance, while the CYGNSS contribution is driven by the climatological anomaly channel and peaks on moderately fast-changing flood scenes. A conditional diffusion model trained as a post-processing module produces calibrated ensemble flood maps with spatially explicit uncertainty estimates, a capability absent from existing operational systems. The framework is designed for direct transfer to the NASA-ISRO NISAR L-band mission, extending applicability to forested tropical floodplains inaccessible to C-band SAR.**

***Index Terms*—CYGNSS, flood mapping, spatio-temporal downscaling, deep learning (DL), SAR, NISAR, uncertainty quantification, MERIT Hydro, GNSS-R**

I. INTRODUCTION

FLOODS rank among the most widespread and damaging natural hazards globally, with direct economic losses estimated at $41 billion annually [1]. As anthropogenic climate change intensifies the hydrological cycle, both the frequency and severity of flood events are projected to increase across tropical and subtropical regions [2]. This trend is already observable from space: satellite observations reveal that the proportion of the global population exposed to floods grew by 20–24% between 2000 and 2015, driven by expanding settlements in floodplains and increasing flood occurrence [3]. Meeting the monitoring demands of this accelerating risk requires flood mapping systems that can operate at daily temporal scales and sub-100 m spatial resolution simultaneously, a combination no existing satellite product currently achieves.

Existing satellite-based flood products face a fundamental spatio-temporal trade-off [4]. GNSS Reflectometry (GNSS-R), as demonstrated by the NASA CYGNSS constellation, offers daily global surface water observations at kilometer-scale spatial resolution [5]–[8]. While this temporal density is invaluable for tracking the dynamic evolution of flood events, the coarse spatial resolution prevents the detection of fine-scale inundation patterns, particularly in fragmented floodplains, agricultural areas, and urban peripheries. Conversely, Synthetic Aperture Radar (SAR) sensors provide high spatial resolution flood maps but with revisit periods of 6 to 12 days, leaving large temporal gaps during rapidly evolving events. Among SAR missions, L-band sensors such as the recently launched NASA-ISRO NISAR mission offer a critical advantage over C-band sensors like Sentinel-1: their longer wavelength allows signal penetration through dense vegetation canopy, enabling flood detection in forested and agricultural areas that C-band cannot reach [9].

Several studies have explored multi-sensor fusion to partially bridge this spatio-temporal gap. Optical–SAR fusion approaches have demonstrated the ability to generate dense time series of surface water extents by combining the cloud-penetration capability of SAR with the spectral richness of optical sensors [10]. While such methods use SAR to fill gaps caused by cloud cover in optical imagery, they still require a valid optical observation to initialize the gap-filling process. Under persistent cloud cover, as is common during the rainy season or flood-inducing weather, the method falls back to SAR alone and remains bound by the 6–12 day revisit cycle, with no independent daily inundation signal available. More recently, deep learning methods applied to SAR data alone have achieved strong performance on large-scale flood benchmarks: Bountos et al. (2023) report F1 scores in the range of 0.78–0.83 on the Kuro Siwo dataset [11], while Misra et al. (2025) demonstrate global-scale flood mapping with IoU = 0.67 across ten years of Sentinel-1 acquisitions [12]. However, these approaches address only one dimension of the trade-off at a time: optical–SAR fusion improves temporal density but does not exploit GNSS-R observations, while SAR-only methods preserve spatial resolution but cannot overcome the 6–12 day revisit constraint. Moreover, none of these approaches provide calibrated uncertainty estimates, a critical gap for operational decision-making where distinguishing high-confidence detections from ambiguous flood boundaries

Gauthier Malandrin is with the École Polytechnique, 91120 Palaiseau, France, and with the Department of Civil and Environmental Engineering, University of California, Berkeley, CA 94720, USA. Cynthia Gerlein-Safdi is with the Dept. of Civil and Environmental Engineering at the University of California, Berkeley, and the Lawrence Berkeley National Laboratory, both located in Berkeley, CA, 94720, USA. *Corresponding author: Cynthia Gerlein-Safdi, cgerlein@berkeley.edu.*

Manuscript received September 2026; revised TBD.

is essential. We address these limitations in the present work.

Here, we propose a physically-constrained deep learning framework for multi-sensor spatio-temporal downscaling of flood maps, fusing daily CYGNSS GNSS-R observations with Sentinel-1 C-band SAR acquisitions as a development proxy for the recently launched NISAR L-band mission. Our model learns to downscale coarse CYGNSS flood signals to 90 m resolution daily flood maps by exploiting temporal triplets of SAR and CYGNSS observations as spatial and temporal anchors, conditioning predictions on high-resolution topographic variables derived from the MERIT Hydro digital elevation model [13], whose 90 m native resolution defines the target grid of our framework. We further extend this deterministic framework with a conditional diffusion model that generates ensembles of plausible flood realizations, yielding spatially explicit uncertainty maps alongside the flood predictions. We validate our approach across seven geographically diverse flood-prone regions spanning three continents, achieving an IoU of 0.703 and exceeding state-of-the-art SAR-only methods despite operating on a harder problem that includes coarse GNSS-R inputs. The proposed architecture is designed to transfer directly to real NISAR L-band data as calibrated acquisitions become available, enabling daily flood mapping at substantially improved spatio-temporal resolution.

II. Background

The use of GNSS Reflectometry for inland flood mapping has expanded rapidly since the launch of the CYGNSS constellation in 2016 [14]. Chew et al. (2018) first demonstrated that CYGNSS data could map flood inundation at higher spatio-temporal resolution than passive microwave radiometers, applying a simple thresholding technique to surface reflectivity observations during Hurricanes Harvey and Irma [5]. Morris et al. (2019) extended this approach to wetland dynamics monitoring, showing that CYGNSS captures seasonal inundation cycles in tropical wetlands including the Everglades [15]. Gerlein-Safdi et al. (2021) used CYGNSS-derived inundation maps to drive methane emission models over the Pantanal and Sudd wetlands, demonstrating the value of frequent L-band observations for tropical wetland hydrology [7]. Beyond inundation mapping, GNSS-R spaceborne observations have demonstrated sensitivity to soil moisture and vegetation [16], and have been applied to soil moisture retrieval using machine learning [17], further establishing the value of L-band reflectometry as a surface hydrology observable. These works established CYGNSS' potential for surface hydrology, but are limited by the coarse spatial resolution inherent to GNSS-R measurements, typically kilometer-scale after spatial averaging, which prevents the detection of fine-scale inundation patterns in fragmented floodplains, agricultural areas, and urban peripheries.

Synthetic Aperture Radar has become the backbone of operational flood mapping due to its all-weather, day-and-night imaging capability [18], and the introduction of these large annotated datasets has enabled deep learning approaches to reach strong performance on flood segmentation benchmarks. Sen1Floods11 [19] introduced the first large georeferenced dataset for training deep learning flood algorithms on Sentinel-1, paving the way for Kuro Siwo, a manually annotated multi-temporal SAR dataset spanning 43 flood events globally, providing baselines achieving F1 scores in the range of 0.78–0.83 on diverse geographic settings [11]. Multi-temporal SAR analysis has also been used to detect floods through harmonic analysis and change detection [20]. Misra et al. (2025) applied a MobileNet-based early fusion change detection model to 10 years of Sentinel-1 data, producing a longitudinal global flood extent dataset and demonstrating real-time disaster response capabilities [12]. Real-time SAR-based flood monitoring has also been demonstrated using Google Earth Engine change detection pipelines [21], and recent methods have further explored nonlocal polarimetric features to improve SAR flood segmentation [22]. While these SAR-only approaches achieve strong performance, they are constrained by the 6–12 day revisit period of individual SAR missions, leaving large temporal gaps during rapidly evolving flood events, and they produce deterministic maps without any uncertainty quantification, a critical limitation for operational flood response where risk managers must distinguish high-confidence detections from ambiguous inundation boundaries.

Several studies have explored multi-sensor data fusion to overcome the individual limitations of each sensor. Markert et al. (2024) proposed a framework combining Sentinel-1 SAR and Landsat-8 optical imagery to generate dense time series of surface water extents through gap filling, achieving improved temporal coverage at the cost of requiring at least one cloud-free optical acquisition to initialize the gap-filling process [10]. Generative approaches have further explored GAN-based fusion of optical and SAR imagery for cloud removal [23], but similarly rely on the availability of a valid optical observation and do not exploit an independent daily inundation signal. Jia et al. (2025) fused CYGNSS data with Sentinel-1 SAR backscatter using machine learning to monitor river water level changes, demonstrating the complementarity of GNSS-R temporal density and SAR spatial resolution [24]. Wang et al. (2025) extended this combination to flood inundation mapping over the contiguous United States, using a two-step Random Forest framework to retrieve daily CYGNSS fractional inundation at 3 km resolution [25]. However, none of these approaches perform explicit spatial downscaling from the CYGNSS resolution to the SAR resolution, nor do they leverage high-resolution topographic variables to guide the spatial disaggregation of the coarse GNSS-R signal, gaps that the present work directly addresses.

Diffusion probabilistic models have recently emerged as a powerful framework for image super-resolution, offering a principled way to generate multiple plausible high-resolution realizations from a single low-resolution input [26]–[28]. Xiao et al. (2023) introduced EDiffSR, an efficient diffusion model for remote sensing image super-resolution using a lightweight conditional U-Net as the denoising backbone [29]. Meng et al. (2024) proposed FastDiffSR, combining a conditional diffusion architecture with an accelerated sampling strategy for high-quality remote sensing super-resolution, achieving faster inference with fewer sampling steps [30]. For Earth observations data fusion, Ibañez et al. (2024) applied a diffusion model to improve the spatial resolution of Sentinel-3 optical products by conditioning on Sentinel-2 high-resolution imagery through a multi-modal loss formulation [31]. In the geosciences, latent diffusion models have been applied to precipitation nowcasting with calibrated uncertainty quantification [32], demonstrating that the generative diversity of diffusion models translates directly to physically meaningful ensemble predictions in Earth observation contexts. These approaches share the key insight that diffusion models naturally capture the distribution of plausible high-resolution images rather than a single deterministic prediction, a property directly applicable to the inherent ambiguity of spatial downscaling in flood mapping.

Building on the complementary strengths identified across these four research directions, the present work proposes a deep learning framework that explicitly learns to downscale daily CYGNSS flood observations from kilometer-scale to 90 m resolution by fusing them with temporal SAR acquisitions used as spatial anchors, conditioned on high-resolution topographic variables from MERIT Hydro. Unlike existing CYGNSS-SAR fusion approaches, our model performs explicit spatial downscaling supervised by real SAR flood masks, trained and validated across seven geographically diverse regions. We further extend this deterministic framework with a conditional diffusion model that provides spatially explicit uncertainty maps alongside flood predictions, a capability not provided by existing operational flood mapping systems.

III. Dataset & Study Areas

Our framework is trained and evaluated across seven geographically and climatologically diverse flood-prone regions spanning three continents: Bangladesh, the Indus floodplain (Pakistan), the Irrawaddy Delta (Myanmar), the Mekong Delta (Vietnam/Cambodia), the Niger Inland Delta (Mali), the Everglades (Florida, USA), and the Mississippi floodplain (USA), as shown in Fig. 1. These regions were selected to maximize diversity in flood dynamics, vegetation cover, and hydrological regimes, from the highly seasonal Niger Inland Delta (mean flood fraction 0.293) to the permanently inundated Everglades (mean flood fraction 0.817) [15]. The dataset spans approximately 752,000 km^2 of flood-prone terrain distributed across these seven regions, computed as the union of per-region non-overlapping bounding boxes derived from the spatial extent of tiles in the catalog. Bangladesh, the Indus floodplain, and the Irrawaddy Delta contribute the largest footprints (166,000, 157,000, and 182,000 km^2 respectively), reflecting their extensive and frequently inundated river systems; model performance is therefore reported separately for each region in Section V to ensure geographic representativeness. All flood observations were taken between 2019 and 2025.

Daily flood observations are derived from the UC Berkeley Random Walk Algorithm WaterMask from CYGNSS (Berkeley-RWAWC) [8], a CYGNSS Level-3 inundation product at $0.01^\circ \times 0.01^\circ$ resolution (1 km at the equator). The product applies a random-walker computer vision algorithm to CYGNSS L-band surface reflectivity observations, exploiting the sensitivity of coherent L-band scattering to surface water even under dense vegetation canopy and persistent cloud cover,

Fig. 1. Geographic distribution of the seven study regions across three continents. Regions were selected to maximize diversity in flood dynamics, vegetation cover, and hydrological regimes, from the highly seasonal Niger Inland Delta to the near-permanently inundated Everglades.

a critical advantage over C-band SAR and optical sensors in tropical environments [7]. For each temporal triplet of the dataset, the CYGNSS watermask corresponding to date B — the central acquisition of the triplet — is used as the primary low-resolution flood signal to be downscaled, while the SAR acquisitions at dates A and C serve as spatial anchors providing high-resolution temporal context.

Flood masks are generated from Sentinel-1 GRD VV backscatter acquisitions processed via Google Earth Engine following standard GRD preprocessing workflows [33], applying a fixed backscatter threshold of -16 dB to discriminate open water from dry land, consistent with threshold values reported in the literature for Sentinel-1 VV flood detection [34], [35]. Flood masks are resampled to 90 m within GEE to match the MERIT Hydro topographic grid, which defines the target resolution of our framework. Binary flood masks serve dual roles in our pipeline — as supervision targets at date B and as spatial anchor inputs at dates A and C, as described in Section IV. We acknowledge that using Sentinel-1 as both temporal anchor and validation target introduces a degree of circularity, which we discuss further in Section VI. Sentinel-1 C-band is used as a development proxy for the NASA-ISRO NISAR L-band mission, whose data products are now becoming available following its launch in 2025. While C-band has known limitations in vegetated areas compared to L-band, it provides the best available high-resolution flood mask archive for training and validation at scale, and our architecture is designed to transfer directly to NISAR L-band data once available.

A key design principle of our framework is to restrict the space of physically plausible flood predictions by conditioning the model on high-resolution topographic information. Flooding is fundamentally constrained by terrain: water accumulates in depressions, follows drainage networks, and is bounded by elevation gradients. Without topographic conditioning, a model trained on coarse CYGNSS observations could produce flood maps that violate basic hydrological consistency. To enforce these physical constraints, we derive four variables from the MERIT Hydro dataset [13], a global hydrography product at 3 arc-second resolution (90 m): the Digital Elevation Model (DEM), the Height Above Nearest Drainage (HAND),

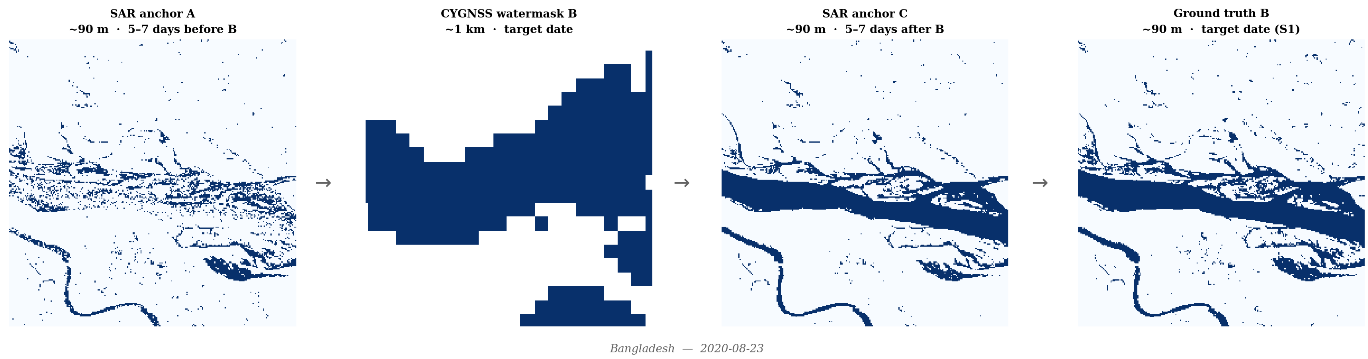

Fig. 2. Example temporal triplet ($A \to B \to C$) for Tile # 08695 over Bangladesh (2020-08-23). From left to right: Sentinel-1 SAR flood mask at date A (5 to 7 days before target date B); CYGNSS watermask at target date B ($\sim$1 km resolution); Sentinel-1 SAR flood mask at date C (5 to 7 days after B); Sentinel-1 "ground truth" at date B, used as training supervision. The coarse pixel structure of the CYGNSS channel contrasts with the 90 m resolution of the SAR channels, illustrating the spatio-temporal gap that the proposed framework bridges.

the log-transformed upstream flow accumulation (ACC_log), which normalizes the highly skewed distribution of drainage area across the study regions, and the Topographic Wetness Index (TWI). HAND in particular encodes the likelihood of inundation based on vertical distance to the nearest drainage network, and has been shown to be a strong predictor of soil water environments and inundation likelihood across diverse hydrological settings [36], [37].

Flood observations are organized as temporal triplets (A $\to$ B $\to$ C), as illustrated in Fig. 2, with gaps of 5 to 7 days between acquisitions, corresponding to the Sentinel-1 revisit period. Dataset construction follows a three-step pipeline. First, flood fractions and SAR coverage are computed for each available date and region; only dates with SAR coverage exceeding 30% of the scene extent and a flood fraction above 5% are retained. Second, valid triplets are assembled from the retained dates; a minimum spacing of 20 days between consecutive triplets is enforced to ensure temporal independence, and a dynamic cap of at most 100 triplets per region — or half the number of unique spatial locations, whichever is smaller — prevents disproportionate over-representation of any single region. Third, 256×256 pixel tiles at 90 m resolution are extracted for each valid triplet, yielding a 10-channel input tensor: four topographic channels (DEM, HAND, ACC_log, TWI), three CYGNSS channels (CYGNSS_B, Mean_CYGNSS, Delta_CYGNSS), and three SAR channels (S1_flood_A, S1_flood_C, Mean_VV). The final dataset comprises 47,653 tiles across 596 unique triplets distributed over the seven study regions. The dataset is split into training (82.9%, 39,505 tiles), validation (9.4%, 4,501 tiles), and test (7.7%, 3,647 tiles) sets at the triplet level to prevent data leakage between temporally adjacent tiles. Splits are stratified by region × season (dry, pre-monsoon, monsoon, post-monsoon): within each region, triplets are grouped by season and independently divided into train/val/test according to fixed ratios of 83/9/8%, ensuring balanced seasonal representation across all three sets and mitigating the flood-fraction bias inherent in year-level splits.

IV. Methodology

A. Temporal Triplet Framework

The core assumption of our framework is that flood extent at a given date can be inferred more accurately by exploiting the temporal context of adjacent SAR acquisitions than by relying on a single observation. We organize flood observations as temporal triplets (A $\to$ B $\to$ C), where B denotes the target date for which we produce a high-resolution flood map, and A and C denote earlier and later SAR acquisitions, respectively, bracketing date B. The gaps between consecutive acquisitions are constrained to 5 to 7 days, corresponding to the Sentinel-1 revisit period, ensuring that the flood state at dates A and C remains informative about conditions at date B without being too distant temporally.

The triplet structure serves two complementary roles. First, the SAR flood masks at dates A and C act as high-resolution spatial anchors: they provide the model with precise information about which areas were flooded immediately before and after the target date, effectively constraining the set of plausible flood extents at date B. Second, the CYGNSS anomaly channel, defined as the difference between the CYGNSS watermask at date B and the long-term regional mean computed over training-set B-date observations for each region, lets the model distinguish background permanent inundation from anomalous flood events. A strongly positive anomaly indicates that date B corresponds to an active flood episode exceeding typical conditions, while a near-zero anomaly suggests stable water levels consistent with the regional climatology. This anomaly signal complements the raw CYGNSS observation by providing a normalized, region-specific flood intensity indicator that is robust to inter-regional differences in baseline inundation levels.

This temporal conditioning strategy is fundamentally different from single-date approaches such as Misra et al. (2025) [12] and the Kuro Siwo benchmark [11], which rely solely on contemporaneous SAR observations. By explicitly providing pre- and post-event context, our model can resolve ambiguous situations where the CYGNSS signal at date B is corrupted by noise, using the SAR anchors to constrain

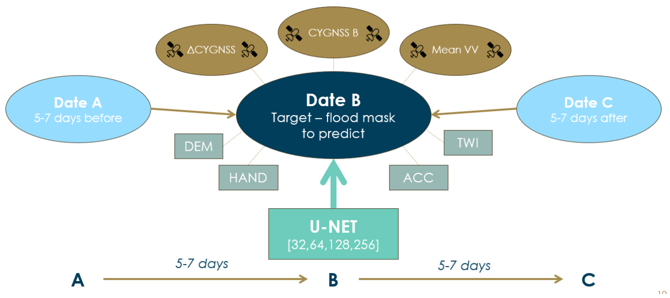

Fig. 3. Overview of the temporal triplet framework. SAR flood masks at dates A and C serve as high-resolution spatial anchors bracketing the target date B by 5 to 7 days. Three CYGNSS channels (CYGNSS_B, ΔCYGNSS, Mean_CYGNSS) provide the daily inundation signal at date B. Four topographic channels derived from MERIT Hydro (DEM, HAND, ACC, TWI) enforce physical consistency. The temporal U-Net fuses these ten channels to produce a 90 m flood probability map at date B.

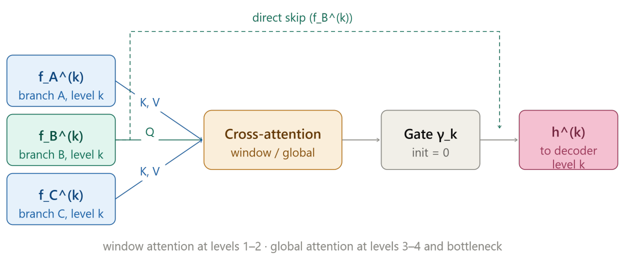

Fig. 4. Detail of the cross-attention skip connection at encoder level k. Features from branches A and C serve as key-value pairs; branch B features serve as query. The gated output fed to the decoder is $h^{(k)} = f_B^{(k)} + \gamma_k \cdot \text{Attn}(f_B^{(k)}, f_A^{(k)}, f_C^{(k)})$, where γ_k is initialized to zero. Window attention is used at levels 1-2; global cross-attention at levels 3-4 and the bottleneck.

the spatial distribution of the downscaled flood prediction, as illustrated in Fig. 3.

B. Model Architecture

We adopt a temporal U-Net architecture as the backbone of our downscaling framework [38], which has demonstrated strong performance on SAR-based flood mapping tasks [39]. Unlike standard U-Nets that process a single input, our architecture maintains three parallel encoding branches, one per temporal acquisition (A, B, C), before merging at the bottleneck via a fusion convolution. This design allows each branch to independently extract spatial features from its respective timestamp before joint reasoning across the triplet. The encoder comprises four levels with feature map sizes [32, 64, 128, 256], followed by a 512-channel bottleneck and a symmetric decoder with transposed convolutions for upsampling. Cross-attention modules are inserted at the skip connections between encoder and decoder: window-based local attention [40], [41] at the two shallowest levels (128×128 and 64×64 feature maps) and global cross-attention at the two deepest levels (32×32 and 16×16), allowing the decoder to selectively attend to temporally relevant features from the anchor acquisitions A and C when reconstructing the flood map at date B. The total number of trainable parameters is 10.55M.

Each cross-attention module incorporates a learnable scalar gate γ_k, initialized to zero, which controls the contribution of the attention output relative to the unmodified skip connection, as detailed in Fig. 4. The output of each attention module at encoder level k is defined as:

$$h^{(k)} = f_B^{(k)} + \gamma_k \cdot \text{Attn}\Big(f_B^{(k)},\, f_A^{(k)},\, f_C^{(k)}\Big) \tag{1}$$

where $f_B^{(k)}$ serves as the query and $f_A^{(k)}$, $f_C^{(k)}$ serve as key-value pairs. γ_k is a learnable scalar gate initialized to zero, providing a smooth bounded scaling (applied as $\tanh(\tilde{\gamma}_k)$ internally). This initialization ensures that the model begins training as a standard U-Net and progressively learns to exploit temporal cross-attention only to the extent supported by the data. To prevent the gate parameters from diverging during training — a pathology observed in preliminary experiments where shallow-level gates saturated at large negative values, effectively disabling the corresponding attention modules — we apply a localized weight decay of $\lambda = 8.94 \cdot 10^{-4}$ to the γ_k parameters exclusively, while leaving all other model weights unregularized. This targeted regularization introduces a restoring force proportional to $|\gamma_k|$ at each gradient step, constraining the gates to moderate values without affecting the learning dynamics of the convolutional layers. In practice, we implement this by splitting the Adam optimizer into two parameter groups with distinct weight-decay coefficients.

Our U-Net takes as input the 10-channel tensor described in Section III, organized into three groups: four topographic channels constraining the space of physically plausible flood predictions, three CYGNSS channels including the climatological anomaly Delta_CYGNSS (provided explicitly to reduce the burden on the optimizer to learn this subtraction implicitly), and three SAR channels comprising the binary flood masks at dates A and C and the long-term mean VV backscatter as a static surface reference.

Each encoding and decoding block consists of two successive 3×3 convolutions followed by Batch Normalization and ReLU activations [42]. MaxPooling with stride 2 is used for downsampling in the encoder. The output layer is a 1×1 convolution producing a single-channel logit map; at inference time, a sigmoid activation yields a spatially explicit flood probability map in [0, 1]. Binary flood masks are obtained by thresholding at 0.5, though the continuous probability output is retained for the diffusion model extension described in Section IV-E.

The choice of [32, 64, 128, 256] features reflects a deliberate trade-off between model capacity and generalization: a larger architecture with [64, 128, 256, 512] features was evaluated during preliminary experiments but showed no significant improvement in validation IoU while requiring approximately 4 times more memory and computation.

All input channels are normalized independently using z-score normalization, with mean and standard deviation computed over the training set. This normalization ensures that channels with very different dynamic ranges, such as ACC_log (spanning several orders of magnitude) and the binary SAR flood masks, contribute comparably to the gradient signal during training.

C. Evaluation Metrics

Flood mapping is inherently a binary segmentation task, and we evaluate model performance using metrics derived from the confusion matrix between predicted and ground truth flood masks. For a given tile, let TP, FP, and FN denote the number of true positive, false positive, and false negative pixels, respectively.

The Intersection over Union (IoU) [12], also known as the Jaccard index, is our primary evaluation metric:

$$\text{IoU} = \frac{TP}{TP + FP + FN} \tag{2}$$

IoU measures the overlap between the predicted flood extent and the ground truth, penalizing both over-prediction (false positives) and under-prediction (false negatives) symmetrically. It is a more stringent metric than accuracy in the context of imbalanced flood scenes, and has become the standard evaluation metric for flood segmentation benchmarks.

We also report Precision and Recall, which capture complementary aspects of model behavior:

$$\text{Precision} = \frac{TP}{TP + FP}, \ \text{Recall} = \frac{TP}{TP + FN} \tag{3}$$

Precision measures the fraction of predicted flood pixels that are truly flooded, while Recall measures the fraction of truly flooded pixels that are correctly detected. These two metrics are in fundamental tension in flood mapping: a model that predicts everything as flooded achieves perfect Recall but zero Precision, while a model that never predicts flooding achieves perfect Precision but zero Recall. The flood-weighted loss described in Section IV-D is designed to encourage the model to maintain high Recall — ensuring that true flood events are not missed — while the IoU metric jointly penalizes deviations in both directions. The F1-score is reported as the harmonic mean of Precision and Recall:

$$\text{F1} = \frac{2 \cdot \text{Precision} \cdot \text{Recall}}{\text{Precision} + \text{Recall}} \tag{4}$$

All metrics are computed at a binarization threshold of 0.5 applied to the model's sigmoid output, and averaged across tiles in the test set. For the probabilistic extension described in Section IV-E, we also report the Expected Calibration Error (ECE) [43] and the Uncertainty-IoU curve, which measure the quality of the predicted uncertainty maps independently of the binary flood detection performance.

D. Training Procedure

The model is trained to minimize a combined Dice and binary cross-entropy loss (Dice+BCE) [44], with a flood-pixel weighting term to address the class imbalance inherent to flood scenes since inundated pixels typically represent between 20% and 50% of a tile depending on the region. The loss is defined as:

$$\mathcal{L} = \alpha \cdot \mathcal{L}_{Dice} + (1 - \alpha) \cdot \mathcal{L}_{BCE}^{w} \tag{5}$$

where $\mathcal{L}_{Dice} = 1 - \frac{2 \sum \hat{y}_{i,j} y_{i,j}}{\sum \hat{y}_{i,j} + \sum y_{i,j}}$ is the Dice loss, and $\mathcal{L}_{BCE}^{w}$ is the flood-weighted binary cross-entropy with a weight of $w = 1.381$ applied to flooded pixels. The Dice loss directly optimizes the IoU-like overlap metric and is less sensitive to class imbalance than standard cross-entropy, making it particularly suited to flood segmentation tasks [45].

Hyperparameters were selected via Bayesian optimization using the Optuna framework [46] over 52 trials of 40 epochs each, including the localized weight decay coefficient λ applied to the γ parameters described in Section IV-B. The optimal configuration found was: $\alpha = 0.620$, flood weight $w = 1.381$, learning rate $\eta = 5.99 \cdot 10^{-5}$, weight decay $\lambda = 8.94 \cdot 10^{-4}$ and batch size 8. Training runs for 300 epochs using the Adam optimizer [47], with a ReduceLROnPlateau scheduler that halves the learning rate when validation IoU fails to improve for 10 consecutive epochs. The best model checkpoint is selected based on maximum validation IoU across all epochs. Data augmentation was disabled following Optuna's recommendation; fANOVA importance analysis over the 52 completed Optuna trials attributed 78% of validation IoU variance to this single hyperparameter decision, which we attribute to the directional nature of the topographic conditioning channels: HAND, flow accumulation, and TWI encode gravity-driven hydrological relationships that random geometric transformations render physically inconsistent.

E. Probabilistic Extension Via Conditional Diffusion Model

While the U-Net described in Section IV-B produces deterministic flood probability maps, operational flood management requires not only a best estimate of flood extent but also a quantification of prediction uncertainty [48]. Ambiguous situations, such as fragmented floodplains or areas at the boundary between flooded and dry land, are precisely where a single deterministic prediction is most likely to be wrong, and where uncertainty information is most valuable for decision-makers.

To address this limitation, we propose a conditional diffusion model as a post-processing module applied on top of the deterministic U-Net predictions. Rather than replacing the U-Net, the diffusion model learns to explore the space of plausible flood realizations consistent with both the deterministic prediction and the original input channels, generating an ensemble of N flood maps from which spatially explicit uncertainty estimates can be derived. This two-stage design preserves the strong deterministic performance of the U-Net while adding a principled probabilistic layer that requires significantly less training time than an end-to-end generative approach.

Diffusion model formulation. Our diffusion model follows the Denoising Diffusion Probabilistic Model (DDPM) framework of Ho et al. (2020) [26], with the cosine noise schedule of Nichol & Dhariwal (2021) [28]. The ground truth binary flood mask, originally in $\{0, 1\}$, is mapped to $\{-1, 1\}$ to center the target distribution around zero — a standard practice in diffusion models that ensures the noise schedule progressively drives the signal toward a symmetric Gaussian distribution $\mathcal{N}(0, I)$ rather than a shifted one [26]. At inference time, outputs are remapped to $[0, 1]$ via $\frac{x_0+1}{2}$. During training, Gaussian noise is progressively added to the remapped flood mask $x_0 \in \{-1, 1\}^{H \times W}$ over $T = 1000$ steps according to :

$$x_t = \sqrt{\bar{\alpha}_t} x_0 + \sqrt{1 - \bar{\alpha}_t} \epsilon, \ \epsilon \sim \mathcal{N}(0, I) \tag{6}$$

where $\bar{\alpha}_t$ follows the cosine schedule. A lightweight conditional U-Net ϵ_θ with architecture [16, 32, 64, 128] (approximately 10 times smaller than the main U-Net) is trained to predict the added noise ϵ given the noisy map x_t, the diffusion timestep t encoded via sinusoidal embeddings, and a 9-channel condition vector c :

$$\mathcal{L}_{diff} = \mathbb{E}_{t,x_0,\epsilon}\left[||\epsilon - \epsilon_\theta(x_t, t_c)||^2\right] \tag{7}$$

The condition vector c concatenates the deterministic U-Net prediction, the raw CYGNSS observation at date B, the four topographic channels, the two SAR spatial anchors at dates A and C, and the CYGNSS anomaly channel Delta_CYGNSS for a total of 9 channels. Mean_CYGNSS and Mean_VV are excluded as their information is already captured by the deterministic U-Net prediction.

Accelerated inference via DDIM and SDEdit. At inference time, we replace the standard DDPM reverse process with Denoising Diffusion Implicit Models (DDIM; Song et al., 2021) [27], achieving comparable sample quality in $S = 50$ steps instead of $T = 1000$, a 20-fold speedup critical for generating large ensembles. Rather than initializing from pure Gaussian noise, we adopt the SDEdit paradigm [49]: the deterministic U-Net prediction $\hat{x}_0$ is first corrupted to noise level $T' = 200$ — approximately 20% of the full diffusion schedule — and the DDIM sampler is then run from T' back to $t = 0$. This preserves the coarse spatial structure of the deterministic prediction while allowing the diffusion model to refine flood boundaries. Sampling from pure noise ($T' = T = 1000$) yielded significantly degraded performance (IoU $= 0.511$ vs IoU $= 0.595$ for $T' = 200$), confirming that SDEdit is essential to maintain spatial coherence with the high-resolution SAR anchors. For each input tile, $N = 20$ independent samples are drawn by initializing from different noise realizations at $T' = 200$.

Uncertainty quantification. From the $N = 20$ samples $\{x_0^{(1)}, x_0^{(2)}, ..., x_0^{(N)}\}$, we derive two outputs. The ensemble mean $\bar{x}_0 = \frac{1}{N}\sum_i x_0^{(i)}$ serves as the probabilistic flood prediction, directly comparable to the deterministic U-Net output in terms of IoU and F1. The pixel-wise standard deviation $\sigma(x_0)$ constitutes the uncertainty map: high values identify pixels where the diffusion model generates inconsistent flood/no-flood predictions across samples, corresponding to genuinely ambiguous regions at flood boundaries, under dense canopy, or in areas of fragmented inundation.

Evaluation metrics for uncertainty. Beyond standard segmentation metrics computed on the ensemble mean, we evaluate the quality of the uncertainty estimates using two dedicated metrics. The Expected Calibration Error (ECE) [43] measures whether predicted flood probabilities are well-calibrated: pixels grouped by predicted probability interval $[\frac{k}{B}, \frac{k+1}{B}]$ should exhibit a true flood frequency close to the interval midpoint. A low ECE indicates that the model is honest about its uncertainty. The Uncertainty-IoU curve measures whether the model knows where it is wrong: by progressively removing pixels with uncertainty $\sigma > \tau$ and recomputing IoU on the retained pixels, we obtain a curve that should rise monotonically if high-uncertainty pixels correspond to model errors. This curve provides an interpretable diagnostic of uncertainty quality that is directly relevant to operational use cases where uncertain predictions can be flagged for human review.

TABLE I
GLOBAL TEST SET PERFORMANCE COMPARISON. METRICS ARE MICRO-AVERAGED OVER ALL PIXELS. DASHES INDICATE METRICS NOT REPORTED IN THE ORIGINAL WORK.

Method	IoU	F1	Precision	Recall
Misra et al. (2025) [12]	0.67	—	—	—
Kuro Siwo best [11]	—	0.83	—	—
This study	**0.703**	**0.826**	0.810	0.842

V. EXPERIMENTAL RESULTS

All metrics are computed as micro-averages, TP and union accumulated over all pixels before taking the ratio, consistent with the aggregation used by Misra et al. (2025) [12] and the Kuro Siwo evaluation protocol [11].

A. Overall Performance

Figure 5 shows the error map obtained for the same tile shown in Fig. 2 and Table I reports test set performance of the proposed framework alongside state-of-the-art flood mapping methods on the 3,647-tile held-out test set. The full model achieves a micro-averaged IoU of 0.703 and F1 of 0.826, outperforming the SAR-only baseline of Misra et al. (2025) [12] (IoU = 0.67) despite operating on a substantially harder problem: rather than segmenting a contemporaneous SAR acquisition, the model must downscale a coarse CYGNSS observation from kilometer scale to 90 m using SAR acquisitions from adjacent dates as spatial anchors, with no contemporaneous high-resolution observation available at the target date. The Kuro Siwo benchmark [11] reports F1 scores of 0.78–0.83 on manually annotated single-event acquisitions; our model achieves F1 = 0.826 on the broader 2019–2025 test set spanning seven diverse regions without event-specific curation, and under automatic Sentinel-1 thresholding rather than manual annotation, a condition that introduces label noise suppressing the reported F1 relative to a manually annotated evaluation. The gap between validation IoU (0.707) and test IoU (0.703) indicates stable generalization across the dataset's temporal and regional diversity.

B. Per-Region Analysis

Figure 6 reports micro-averaged IoU decomposed by region. Performance varies substantially, reflecting differences in flood dynamics, vegetation cover, and reference mask quality. Bangladesh (IoU = 0.787, n = 921) and the Everglades (IoU = 0.884, n = 61) achieve the strongest results: Bangladesh combines large contiguous inundation extents with dense Sentinel-1 coverage, while the Everglades is a near-permanently inundated wetland where the CYGNSS anomaly signal is consistently informative. The Mekong Delta (IoU = 0.641, n = 794) and the Indus floodplain (IoU = 0.558, n = 483) underperform compared to the global average; Indus performance is structurally low across all years (0.51–0.60),

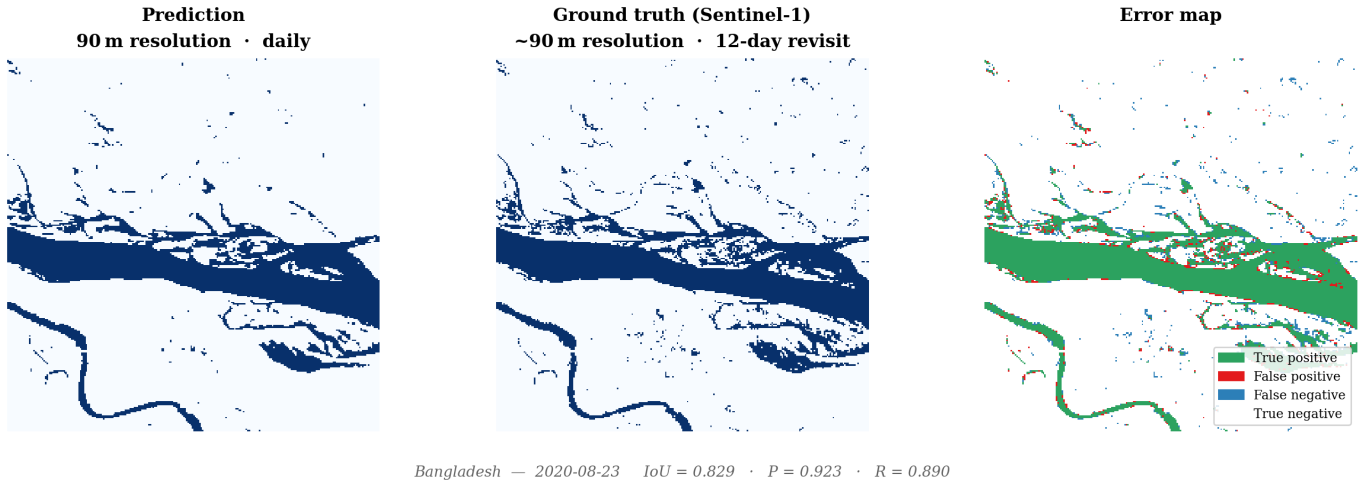

Fig. 5. Qualitative results on Tile # 08695, Bangladesh (2020-08-23). *Left:* model prediction at 90 m resolution (daily). *Centre:* Sentinel-1 ground truth at ∼90 m resolution (12-day revisit). *Right:* pixel-wise error map (green = true positive, red = false positive, blue = false negative, white = true negative). IoU = 0.829, Precision = 0.923, Recall = 0.890 for this tile. Errors concentrate on channel edges and fragmented inundation patches where the fixed −16 dB Sentinel-1 threshold partially misses fine-scale flood boundaries.

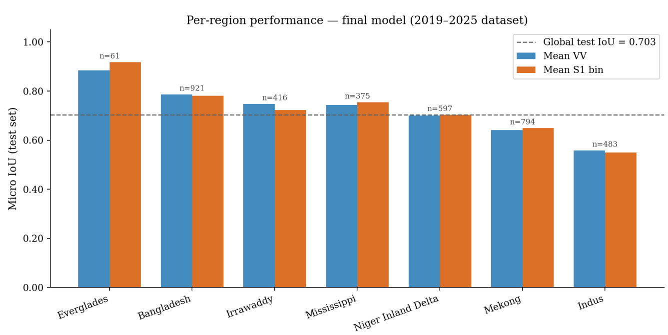

Fig. 6. Per-region micro-averaged IoU on the 3,647-tile test set. Blue bars: `Mean_VV` variant (published model); orange bars: `Mean_S1_binary` variant. The dashed line indicates the global test IoU of 0.703. Region sample sizes (n) are indicated above each bar pair. The Everglades result ($n = 61$) should be interpreted with caution given the limited test set size.

TABLE II
FULL ABLATION STUDY. MICRO-AVERAGED IOU ON THE 3,647-TILE TEST SET. CHANNELS OUTSIDE EACH CONFIGURATION ARE SET TO ZERO (TRAINING-SET MEAN AFTER Z-SCORE NORMALIZATION). ALL CONFIGURATIONS USE 150-EPOCH TRAINING; THE PUBLISHED RESULT (300 EPOCHS, CONFIG E) IS WITHIN 0.001 OF THE 150-EPOCH CONTROL.

Config	Input channels	IoU	Δ vs A
A	Topography only	0.590	—
B	Topo + CYGNSS_B + Mean_CYGNSS	0.565	−0.025
C	Topo + CYGNSS_B + Mean_CYGNSS + SAR	0.686	+0.096
D	Topo + Full CYGNSS + SAR	0.703	+0.113
E	Full model (all modalities)	0.702	+0.112
F	Topo + CYGNSS_B + SAR	0.692	+0.102
G	Topo + SAR only	0.695	+0.105
H	Topo + Full CYGNSS (no SAR)	0.577	−0.013

suggesting a systematic limitation linked to fragmented agricultural inundation patterns and complex drainage networks that are poorly captured at both CYGNSS and 90 m SAR resolution.

C. Ablation Study

To quantify the respective contributions of topographic conditioning, CYGNSS observations, and SAR temporal anchors, we conduct a structured ablation study across seven input configurations. We set channels outside each configuration to zero rather than remove them, preserving the 10-channel input dimensionality and the three-branch temporal architecture across all configurations. Since tiles are z-scored at creation time, zero corresponds to the training-set mean, the standard non-informative substitute, ensuring that only the available information varies between configurations.

Table II reports micro-averaged IoU for all seven configurations. SAR temporal anchors are the dominant input modality, contributing +0.105 IoU over the topographic baseline (config. G vs A), by far the largest single gain, consistent across all dataset versions evaluated. CYGNSS observations alone (config. H) degrade performance below the topographic baseline (−0.013 IoU): the raw CYGNSS signal at kilometer scale cannot be spatially disaggregated without a high-resolution spatial reference, and topography alone resolves the spatial ambiguity more effectively. The full model achieves a net CYGNSS gain of +0.007 over the SAR-only configuration (config. E vs G), confirming that CYGNSS is informative only when SAR anchors constrain its spatial interpretation. Comparing configs C and D isolates the contribution of the Delta_CYGNSS anomaly channel: removing it while retaining CYGNSS_B and Mean_CYGNSS reduces IoU from 0.703 to 0.686, demonstrating that the model exploits deviation from regional climatology rather than absolute inundation level.

D. CYGNSS Contribution Stratified by Flood Dynamics

To test whether the CYGNSS gain concentrates on rapidly evolving flood events, where the 6–12 day SAR revisit leaves

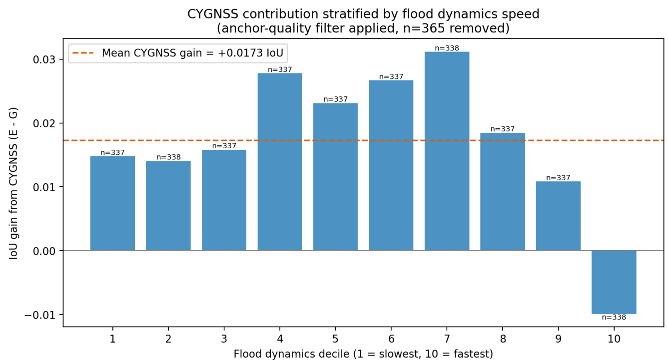

Fig. 7. CYGNSS gain (E−G, micro-averaged IoU) across ten equal-sized deciles of δ_{SAR} on the 3,282 retained tiles (365 tiles excluded by anchor coherence filter). Positive values indicate that the full model outperforms the SAR-only baseline. The gain is positive on deciles D1–D9 and peaks at +0.031 on D7; the negative value on D10 is attributable to residual anchor-quality issues at the highest inter-anchor incoherence values. The red dashed line indicates the mean gain of +0.017 IoU across deciles.

the largest information gap, we stratify the test set by a proxy of flood dynamics speed:

$$\delta_{\text{SAR}} = \text{mean}(|\texttt{S1\_flood\_A} - \texttt{S1\_flood\_C}|) \tag{8}$$

The fraction of pixels whose flood state changed between the two SAR anchor dates. Prior to stratification, 365 tiles (10.0% of the test set) exhibiting hydrologically implausible inter-anchor configurations (IoU(A,C) < 0.05 while Union(A,C) > 0.30, concentrated in the Mekong in 2021) are excluded via an anchor coherence filter.

Fig. 7 shows the CYGNSS gain (E−G) across ten equal-sized deciles of δ_{SAR} on the 3,282 retained tiles, where $\delta_{\text{SAR}} = \text{mean}(|\text{S1\_flood\_A} - \text{S1\_flood\_C}|)$ denotes the mean absolute pixel-wise difference between the two SAR anchors and serves as a proxy for flood dynamics speed. The gain is positive on 9 out of 10 deciles, with a mean of +0.017 IoU across deciles and a peak of +0.031 on decile D7 (median $\delta_{\text{SAR}} = 0.076$). The negative value on D10 (−0.010) is attributable to residual anchor-quality issues at the highest inter-anchor incoherence values. These results confirm that CYGNSS provides consistent improvement across the full spectrum of flood dynamics captured in the dataset, with concentration in the moderate-to-fast regime where inter-anchor disagreement signals genuine hydrological change rather than data artifacts, precisely the operational scenario where daily GNSS-R observations are most valuable.

TABLE III
DETERMINISTIC U-NET VS. DIFFUSION ENSEMBLE ON THE TEST SET. IOU IS MICRO-AVERAGED OVER ALL PIXELS; ECE IS THE EXPECTED CALIBRATION ERROR COMPUTED OVER ALL TEST PIXELS; σ IS THE MEAN PIXEL-WISE STANDARD DEVIATION ACROSS THE ENSEMBLE.

Method	**IoU**	**ECE**	**Mean σ**
U-Net (deterministic)	0.703	—	—
Diffusion ensemble ($N = 20$)	0.665	0.073	0.023

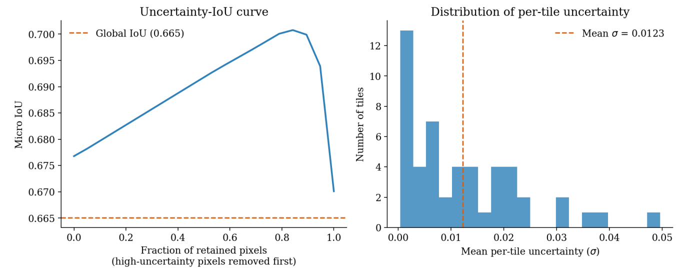

Fig. 8. Uncertainty-IoU curve computed on a 50-tile random sample of the test set ($N = 3$ diffusion samples per tile, $S = 20$ DDIM steps, $T_{\text{start}} = 200$). IoU peaks at 0.700 when the most uncertain 20% of pixels are removed (fraction of retained pixels = 0.8), compared to IoU = 0.677 at full pixel retention, confirming that high-uncertainty pixels correspond systematically to model errors. The dashed line indicates the global diffusion ensemble IoU (0.665, $N = 20$).

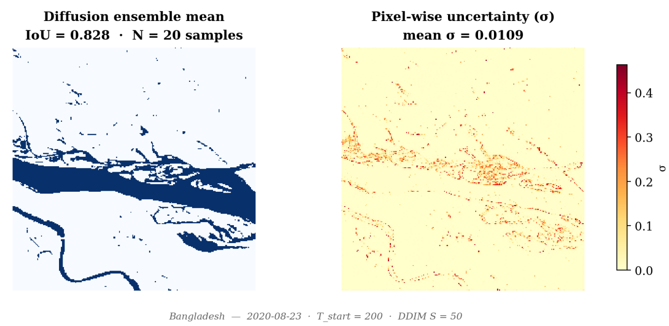

Fig. 9. Diffusion ensemble results on Tile # 08695, Bangladesh (2020-08-23; $T_{\text{start}} = 200$, DDIM $S = 50$, $N = 20$ samples). *Left:* ensemble mean prediction (IoU = 0.828). *Right:* pixel-wise uncertainty map (σ; mean $\bar{\sigma} = 0.0109$). High-uncertainty pixels concentrate on flood boundaries and fragmented inundation patches, confirming that the diffusion model correctly localizes the regions where the deterministic U-Net is most likely to err.

E. Probabilistic Flood Mapping

Table III summarizes the performance of the diffusion ensemble against the deterministic U-Net baseline. The diffusion ensemble achieves an IoU of 0.665, below the U-Net baseline of 0.703; this gap is expected since the SDEdit initialization constrains the ensemble output to remain close to the U-Net prediction, so systematic errors in the U-Net propagate into the ensemble mean. The primary contribution of the diffusion component is not improved point-estimate accuracy but spatially calibrated uncertainty quantification: the ECE of 0.073 indicates well-calibrated ensemble probabilities, and the Uncertainty-IoU curve rises monotonically from IoU = 0.677 at full pixel retention to a peak of IoU = 0.700 (see Fig. 8), when the most uncertain 20% of pixels are removed — confirming that high-uncertainty pixels correspond systematically to model errors. The mean pixel-wise uncertainty $\sigma = 0.023$ confirms that uncertainty concentrates on a small fraction of pixels (flood boundaries and fragmented inundation patches) rather than being diffuse across the map, as exemplified in Fig. 9. The 50-tile diagnostic sample used to compute the Uncertainty-IoU curve yields a consistent mean $\sigma = 0.0123$, close to the full test-set value of $\bar{\sigma} = 0.023$ reported in Table III; the difference reflects the smaller sample size and its regional composition rather than indicating a distributional inconsistency.

VI. Discussion

A. Benchmark Comparison and Positioning

The proposed framework achieves IoU = 0.703, outperforming the SAR-only baseline of Misra et al. (2025) [12] by +0.033 while solving a strictly harder problem: spatial downscaling from kilometer-scale CYGNSS inputs rather than segmentation of a contemporaneous SAR acquisition. The structured ablation shows this performance is not simply an artifact of SAR temporal interpolation: CYGNSS contributes a measurable, physically interpretable gain of +0.007 globally and +0.017 mean across flood-dynamics deciles on the filtered test set, driven by the climatological anomaly channel rather than the raw watermask. Our model is the first to demonstrate that explicit spatial downscaling from GNSS-R to SAR resolution, supervised by real flood masks across seven diverse regions, can exceed state-of-the-art SAR-only performance.

B. Limitations

Four limitations warrant explicit discussion. First, using Sentinel-1 as both the spatial anchor modality and the validation target introduces circularity into the evaluation: the model learns to interpolate between two Sentinel-1 observations and is assessed against a third observation of the same surface. This circularity is partially mitigated by the 5–7 day temporal gap between anchor and target acquisitions, and by the ablation demonstrating an independent CYGNSS contribution; nonetheless, a fully independent validation against field-based observations, such as USGS High Water Mark records, would strengthen the benchmark. However, such datasets are extremely rare, and their format and quality are highly variable, making such datasets impossible to use as a training set.

Second, the dataset pipeline contains a residual anchor coherence issue (10% of test tiles, concentrated in the Mekong in 2021) that likely suppresses the measured CYGNSS gain in the highest δ_{SAR} decile. Integrating an anchor coherence filter in future dataset iterations is straightforward and expected to improve performance on affected region-year combinations.

Third, the Indus floodplain presents structurally low performance (IoU = 0.51–0.60) across all years. We hypothesize that this reflects small-scale, fragmented inundation patterns driven by irrigation management rather than natural hydrological dynamics, a regime where both CYGNSS and 90 m SAR lack the spatial resolution to capture field-scale water extents, and where MERIT Hydro topographic conditioning provides limited guidance in the absence of a well-defined drainage network.

Finally, while the Sentinel-1 C-band anchor is known to be attenuated by dense vegetation canopy [9], our analysis does not reveal a systematic CYGNSS-specific bias under forest cover. Fig. 10 stratifies model performance and CYGNSS gain (E−G) by forest cover decile derived from the Hansen Global Forest Change dataset. The full model and the SAR-only ablation exhibit nearly identical IoU degradation as forest cover increases (left panel), confirming that the shared C-band limitation affects both modalities equally. The CYGNSS gain (right panel) shows no monotonic trend with forest cover: it is positive in low-to-moderate canopy deciles (D1–D3, D5–D6) and near zero in the densest deciles (D8–D10), but this attenuation mirrors the anchor quality degradation rather than a CYGNSS-specific sensitivity loss under C-band-attenuated canopy. These results suggest that transferring the framework to NISAR L-band, where canopy penetration is substantially improved, should benefit both anchor quality and spatial disaggregation of the CYGNSS signal jointly, rather than resolving a CYGNSS-only bottleneck.

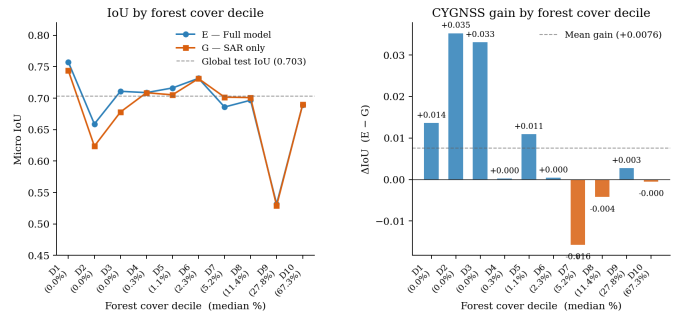

Fig. 10. IoU and CYGNSS gain (E−G) stratified by forest cover decile (Hansen Global Forest Change tree cover, median % per decile). *Left:* micro-averaged IoU for the full model (E) and the SAR-only ablation (G) across deciles. *Right:* CYGNSS gain per decile; the mean gain of +0.0076 IoU (dashed line) is positive across D1–D3 and D5–D6 but near zero or negative in the densely forested deciles D7–D10. The absence of a monotonic negative trend with forest cover confirms that the performance gap in forested regions reflects SAR C-band limitations shared by both E and G, rather than a CYGNSS-specific bias: the CYGNSS contribution is not suppressed by canopy and is not structured by forest cover.

C. Transfer to NISAR L-band Data and future GNSS-R missions

We developed the framework using Sentinel-1 C-band SAR as a proxy for the NASA-ISRO NISAR L-band mission, which launched in July 2025 and for which calibrated science-quality data products are now becoming available. The proposed architecture requires no modification to operate on NISAR data: the three SAR input channels need only be replaced with their NISAR L-band equivalents, derived using a backscatter threshold appropriate for L-band open water detection. This transition offers two benefits: at 24 cm wavelength, L-band SAR detects double-bounce scattering between floodwater and tree trunks [50], making it sensitive to inundation beneath tropical forest cover where C-band is partially attenuated [9], extending the framework's geographic validity to the Amazon basin, the Congo floodplain, and the Irrawaddy Delta, precisely the regions where daily CYGNSS monitoring provides the greatest operational value. Additionally, in operational deployment, no SAR acquisition is needed at the target date B: any date between two consecutive acquisitions A and C can serve as a target, effectively halving the inter-anchor window from 10–14 days (training constraint) to 5–7 days and providing genuinely continuous daily flood mapping between SAR overpasses.

Additionally, CYGNSS is currently scheduled for decommissioning by the end of December 2026. However, we expect the growing ecosystem of GNSS-R missions launched by both space agencies and private companies [51] to supply a steady stream of GNSS-R data that could be used to produce daily watermasks once CYGNSS data is no longer available. These new missions, most of which have polar orbits, would let us expand the method proposed here beyond CYGNSS' tropical band and into boreal ecosystems, where faster-than-average warming is rapidly changing wetland dynamics and their contribution to the global methane budget.

VII. How to Use Our Model

The code and pre-trained weights are available at github.com/gauthiermalandrin1903/cygnss-sar-flood-mapping, with weights hosted on HuggingFace at huggingface.co/gauthiermalandrin/cygnss-sar-flood-mapping and downloaded automatically on first use. We provide four recommendations for users applying the framework to new regions or flood events.

Triplet construction. The model requires two Sentinel-1 acquisitions (A, C) bracketing the target date B by 5–7 days, along with the CYGNSS watermask at B. No SAR acquisition is needed at B itself — inferring flood extent at the target date from surrounding anchors is precisely the problem the model solves.

CYGNSS anomaly channel. The CYGNSS contribution is driven primarily by the climatological anomaly ΔCYGNSS (Section V-C). Providing the long-term regional mean watermask via `mean_cygnss` is strongly recommended; when omitted, this channel defaults to zero and performance on rapidly evolving flood events will be reduced.

Uncertainty quantification. The `EnsemblePredictor` class generates $N = 20$ diffusion samples and returns a pixel-wise uncertainty map alongside the flood prediction, enabling high-uncertainty pixels to be flagged for human review.

Geographic transferability. Performance may be reduced in regions with fragmented agricultural inundation driven by irrigation management — a systematic challenge identified on the Indus floodplain (IoU = 0.51–0.60). Independent validation against field observations is recommended when applying the model to new geographic settings.

VIII. Conclusion

We presented a physically-constrained deep learning framework for daily flood mapping at 90 m resolution through spatio-temporal fusion of CYGNSS GNSS-R observations and Sentinel-1 SAR temporal anchors, conditioned on high-resolution topographic variables derived from MERIT Hydro. Trained and evaluated on a 47,653-tile dataset spanning seven geographically diverse flood-prone regions across three continents and seven years, the proposed temporal U-Net achieves a micro-averaged IoU of 0.703 on the held-out test set, outperforming the state-of-the-art SAR-only baseline despite solving a substantially harder downscaling problem. A structured ablation study shows that SAR temporal anchors dominate performance, while the CYGNSS contribution, driven entirely by the climatological anomaly channel, is most pronounced on moderately fast-changing flood scenes. A conditional diffusion model trained as a post-processing module adds spatially calibrated uncertainty quantification absent from existing operational flood mapping systems. The framework is designed for direct transfer to NISAR L-band data, extending its geographic validity to forested tropical floodplains currently inaccessible to C-band SAR.

References

[1] S. Mtibaa, K. Maeno, K. Islam, and M. Motoshita, "Potential risk by riverine floods in the global economy: Sector-wise assessment of direct and indirect impacts through international trade," *Journal of Environmental Management*, vol. 393, p. 127041, 2025.

[2] Y. Hirabayashi, R. Mahendran, S. Koirala, L. Konoshima, D. Yamazaki, S. Watanabe, H. Kim, and S. Kanae, "Global flood risk under climate change," *Nature climate change*, vol. 3, no. 9, pp. 816–821, 2013.

[3] B. Tellman, J. A. Sullivan, C. Kuhn, A. J. Kettner, C. S. Doyle, G. R. Brakenridge, T. A. Erickson, and D. A. Slayback, "Satellite imaging reveals increased proportion of population exposed to floods," *Nature*, vol. 596, no. 7870, pp. 80–86, 2021.

[4] J.-F. Pekel, A. Cottam, N. Gorelick, and A. S. Belward, "High-resolution mapping of global surface water and its long-term changes," *Nature*, vol. 540, no. 7633, pp. 418–422, 2016.

[5] C. Chew, J. T. Reager, and E. Small, "Cygnss data map flood inundation during the 2017 atlantic hurricane season," *Scientific reports*, vol. 8, no. 1, p. 9336, 2018.

[6] C. Gerlein-Safdi and C. S. Ruf, "A cygnss-based algorithm for the detection of inland waterbodies," *Geophysical Research Letters*, vol. 46, no. 21, pp. 12 065–12 072, 2019.

[7] C. Gerlein-Safdi, A. A. Bloom, G. Plant, E. A. Kort, and C. S. Ruf, "Improving representation of tropical wetland methane emissions with cygnss inundation maps," *Global Biogeochemical Cycles*, vol. 35, no. 12, p. e2020GB006890, 2021.

[8] T. Pu, C. Gerlein-Safdi, Y. Xiong, M. Li, E. A. Kort, and A. A. Bloom, "Berkeley-rwawc: A new cygnss-based watermask unveils unique observations of seasonal dynamics in the tropics," *Water Resources Research*, vol. 60, no. 7, p. e2024WR037060, 2024.

[9] E. Ramsey III, A. Rangoonwala, and T. Bannister, "Coastal flood inundation monitoring with satellite c-band and l-band synthetic aperture radar data," *JAWRA Journal of the American Water Resources Association*, vol. 49, no. 6, pp. 1239–1260, 2013.

[10] K. N. Markert, G. P. Williams, E. J. Nelson, D. P. Ames, H. Lee, and R. E. Griffin, "Dense time series generation of surface water extents through optical–sar sensor fusion and gap filling," *Remote Sensing*, vol. 16, no. 7, p. 1262, 2024.

[11] N. I. Bountos, M. Sdraka, A. Zavras, I. Karasante, A. Karavias, T. Herekakis, A. Thanasou, D. Michail, and I. Papoutsis, "Kuro siwo: 33 billion m^2 under the water. a global multi-temporal satellite dataset for rapid flood mapping," *arXiv preprint arXiv:2311.12056*, 2023.

[12] A. Misra, K. White, S. F. Nsutezo, W. Straka III, and J. Lavista, "Mapping global floods with 10 years of satellite radar data," *Nature Communications*, vol. 16, no. 1, p. 5762, 2025.

[13] D. Yamazaki, D. Ikeshima, J. Sosa, P. D. Bates, G. H. Allen, and T. M. Pavelsky, "Merit hydro: A high-resolution global hydrography map based on latest topography dataset," *Water Resources Research*, vol. 55, no. 6, pp. 5053–5073, 2019.

[14] C. S. Ruf, R. Atlas, P. S. Chang, M. P. Clarizia, J. L. Garrison, S. Gleason, S. J. Katzberg, Z. Jelenak, J. T. Johnson, S. J. Majumdar *et al.*, "New ocean winds satellite mission to probe hurricanes and tropical convection," *Bulletin of the American Meteorological Society*, vol. 97, no. 3, pp. 385–395, 2016.

[15] M. Morris, C. Chew, J. T. Reager, R. Shah, and C. Zuffada, "A novel approach to monitoring wetland dynamics using cygnss: Everglades case study," *Remote Sensing of Environment*, vol. 233, p. 111417, 2019.

[16] A. Camps, H. Park, M. Pablos, G. Foti, C. P. Gommenginger, P.-W. Liu, and J. Judge, "Sensitivity of gnss-r spaceborne observations to soil moisture and vegetation," *IEEE Journal of Selected Topics in Applied Earth Observations and Remote Sensing*, vol. 9, no. 10, pp. 4730–4742, 2016.

[17] Y. Jia, S. Jin, P. Savi, Y. Gao, J. Tang, Y. Chen, and W. Li, "Gnss-r soil moisture retrieval based on a xgboost machine learning aided method: Performance and validation," *Remote sensing*, vol. 11, no. 14, p. 1655, 2019.

[18] D. Amitrano, G. Di Martino, A. Di Simone, and P. Imperatore, "Flood detection with sar: A review of techniques and datasets," *Remote Sensing*, vol. 16, no. 4, p. 656, 2024.

[19] D. Bonafilia, B. Tellman, T. Anderson, and E. Issenberg, "Sen1floods11: A georeferenced dataset to train and test deep learning flood algorithms for sentinel-1," in *2020 IEEE/CVF conference on computer vision and pattern recognition workshops (CVPRW)*. IEEE, 2020, pp. 835–845.

[20] S. Schlaffer, P. Matgen, M. Hollaus, and W. Wagner, "Flood detection from multi-temporal sar data using harmonic analysis and change detection," *International Journal of Applied Earth Observation and Geoinformation*, vol. 38, pp. 15–24, 2015.

[21] E. Hamidi, B. G. Peter, D. F. Muñoz, H. Moftakhari, and H. Moradkhani, "Fast flood extent monitoring with sar change detection using google earth engine," *IEEE Transactions on Geoscience and Remote Sensing*, vol. 61, pp. 1–19, 2023.

[22] H. Zhuang, P. Wang, M. Hao, H. Fan, and Z. Tan, "Flood inundation mapping in sar images based on nonlocal polarization combination features," *Journal of Hydrology*, vol. 646, p. 132326, 2025.

[23] J. Gao, Q. Yuan, J. Li, H. Zhang, and X. Su, "Cloud removal with fusion of high resolution optical and sar images using generative adversarial networks," *Remote Sensing*, vol. 12, no. 1, p. 191, 2020.

[24] Y. Jia, Q. Liu, C. Song, Z. Xiao, Q. Dai, S. Jin, and P. Savi, "Fusing sar image and cygnss data for monitoring river water level changes by machine learning," *Remote Sensing of Environment*, vol. 329, p. 114927, 2025.

[25] H. Wang, F. Lei, X. Shen, Q. Yang, E. N. Anagnostou, W. T. Crow, H. Kim, and C. Chew, "Flood inundation mapping with cygnss over conus: a two-step machine-learning-based framework," *Journal of Hydrology*, p. 134224, 2025.

[26] J. Ho, A. Jain, and P. Abbeel, "Denoising diffusion probabilistic models," *Advances in neural information processing systems*, vol. 33, pp. 6840–6851, 2020.

[27] J. Song, C. Meng, and S. Ermon, "Denoising diffusion implicit models," *arXiv preprint arXiv:2010.02502*, 2020.

[28] A. Q. Nichol and P. Dhariwal, "Improved denoising diffusion probabilistic models," in *International conference on machine learning*. PMLR, 2021, pp. 8162–8171.

[29] Y. Xiao, Q. Yuan, K. Jiang, J. He, X. Jin, and L. Zhang, "Ediffsr: An efficient diffusion probabilistic model for remote sensing image super-resolution," *IEEE Transactions on Geoscience and Remote Sensing*, vol. 62, pp. 1–14, 2023.

[30] F. Meng, Y. Chen, H. Jing, L. Zhang, Y. Yan, Y. Ren, S. Wu, T. Feng, R. Liu, and Z. Du, "A conditional diffusion model with fast sampling strategy for remote sensing image super-resolution," *IEEE Transactions on Geoscience and Remote Sensing*, vol. 62, pp. 1–16, 2024.

[31] D. Ibañez, R. Fernandez-Beltran, F. Pla, N. Yokoya, and J. Xia, "Multimodal consistent loss diffusion model for sentinel-3 single image super resolution," *Neural Computing and Applications*, vol. 37, no. 10, pp. 7121–7143, 2025.

[32] J. Leinonen, U. Hamann, D. Nerini, U. Germann, and G. Franch, "Latent diffusion models for generative precipitation nowcasting with accurate uncertainty quantification," *arXiv preprint arXiv:2304.12891*, 2023.

[33] F. Filipponi, "Sentinel-1 grd preprocessing workflow," in *Proceedings*, vol. 18, no. 1. MDPI, 2019, p. 11.

[34] C. Bayik, S. Abdikan, G. Ozbulak, T. Alasag, S. Aydemir, and F. Balik Sanli, "Exploiting multi-temporal sentinel-1 sar data for flood extend mapping," *The international archives of the photogrammetry, remote sensing and spatial information sciences*, vol. 42, pp. 109–113, 2018.

[35] A. Twele, W. Cao, S. Plank, and S. Martinis, "Sentinel-1-based flood mapping: a fully automated processing chain," *International Journal of Remote Sensing*, vol. 37, no. 13, pp. 2990–3004, 2016.

[36] A. D. Nobre, L. A. Cuartas, M. Hodnett, C. D. Rennó, G. Rodrigues, A. Silveira, and S. Saleska, "Height above the nearest drainage–a hydrologically relevant new terrain model," *Journal of Hydrology*, vol. 404, no. 1-2, pp. 13–29, 2011.

[37] O. E. Wing, P. D. Bates, C. C. Sampson, A. M. Smith, K. A. Johnson, and T. A. Erickson, "Validation of a 30 m resolution flood hazard model of the conterminous u nited s tates," *Water Resources Research*, vol. 53, no. 9, pp. 7968–7986, 2017.

[38] O. Ronneberger, P. Fischer, and T. Brox, "U-net: Convolutional networks for biomedical image segmentation," in *International Conference on Medical image computing and computer-assisted intervention*. Springer, 2015, pp. 234–241.

[39] G. Konapala, S. V. Kumar, and S. K. Ahmad, "Exploring sentinel-1 and sentinel-2 diversity for flood inundation mapping using deep learning," *ISPRS Journal of Photogrammetry and Remote Sensing*, vol. 180, pp. 163–173, 2021.

[40] Z. Liu, Y. Lin, Y. Cao, H. Hu, Y. Wei, Z. Zhang, S. Lin, and B. Guo, "Swin transformer: Hierarchical vision transformer using shifted windows," in *Proceedings of the IEEE/CVF international conference on computer vision*, 2021, pp. 10 012–10 022.

[41] H. Chen, Z. Qi, and Z. Shi, "Remote sensing image change detection with transformers," *IEEE Transactions on Geoscience and Remote Sensing*, vol. 60, pp. 1–14, 2021.

[42] S. Ioffe and C. Szegedy, "Batch normalization: Accelerating deep network training by reducing internal covariate shift," in *International conference on machine learning*. pmlr, 2015, pp. 448–456.

[43] C. Guo, G. Pleiss, Y. Sun, and K. Q. Weinberger, "On calibration of modern neural networks," in *International conference on machine learning*. PMLR, 2017, pp. 1321–1330.

[44] S. Jadon, "A survey of loss functions for semantic segmentation," in *2020 IEEE conference on computational intelligence in bioinformatics and computational biology (CIBCB)*. IEEE, 2020, pp. 1–7.

[45] F. Milletari, N. Navab, and S.-A. Ahmadi, "V-net: Fully convolutional neural networks for volumetric medical image segmentation," in *2016 fourth international conference on 3D vision (3DV)*. Ieee, 2016, pp. 565–571.

[46] T. Akiba, S. Sano, T. Yanase, T. Ohta, and M. Koyama, "Optuna: A next-generation hyperparameter optimization framework," in *Proceedings of the 25th ACM SIGKDD international conference on knowledge discovery & data mining*, 2019, pp. 2623–2631.

[47] D. P. Kingma and J. Ba, "Adam: A method for stochastic optimization," *arXiv preprint arXiv:1412.6980*, 2014.

[48] A. Kendall and Y. Gal, "What uncertainties do we need in bayesian deep learning for computer vision?" *Advances in neural information processing systems*, vol. 30, 2017.

[49] C. Meng, Y. He, Y. Song, J. Song, J. Wu, J.-Y. Zhu, and S. Ermon, "Sdedit: Guided image synthesis and editing with stochastic differential equations," *arXiv preprint arXiv:2108.01073*, 2021.

[50] J.-M. Martinez and T. Le Toan, "Mapping of flood dynamics and spatial distribution of vegetation in the amazon floodplain using multitemporal sar data," *Remote sensing of Environment*, vol. 108, no. 3, pp. 209–223, 2007.

[51] C. Ruf and S. Gleason, "Spaceborne GNSS-R Bistatic Radar Remote Sensing, CYGNSS, and Future Missions," *Proceedings of the IEEE*, vol. 114, no. 2, pp. 308–326, 2026.

Gauthier Malandrin is currently pursuing the M.Eng degree at École Polytechnique, Palaiseau, France. He was a Visiting Scholar in Prof. Gerlein-Safdi's Research Group at the University of California, Berkeley, CA, USA, in Spring and Summer 2026. His studies focus on aerospace-related science and machine learning.

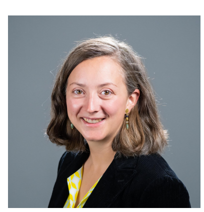

Cynthia Gerlein-Safdi (Member, IEEE) received the bachelor's degree in Geosciences from the University of Strasbourg, France, in 2009, the MEng degree in Geophysical Engineering from the École et Observatoire des Sciences de la Terre, Strasbourg, France, in 2012, and the PhD degree in Civil and Environmental Engineering from Princeton University, Princeton, NJ, USA, in 2017. She is currently an Assistant Professor in Civil and Environmental Engineering at UC Berkeley, CA, USA. Her research interests include ecohydrology, understanding the links between the water and carbon cycles, and remote sensing of water and vegetation.